PHYSICAL REVIEW B **96**, 100405(R) (2017)

Real-space observation of nanoscale magnetic phase separation in dysprosium by aberration-corrected Lorentz microscopy

Takuro Nagai,[1] Koji Kimoto,[1] Koji Inoke,[2] and Masaki Takeguchi[1]
[1]*National Institute for Materials Science (NIMS), Tsukuba, Ibaraki 305-0044, Japan*
[2]*FEI Company Japan Ltd., Kohnan, Tokyo 108-007, Japan*

(Received 2 June 2017; revised manuscript received 9 August 2017; published 19 September 2017)

Magnetic phase separation in single-crystal dysprosium at 97–187 K was investigated using aberration-corrected Lorentz microscopy. The high-resolution Lorentz microscopy combined with the transport-of-intensity equation method successfully visualized the in-plane magnetization distribution of the coexisting magnetic phases. The onset of a phase transition from the ferromagnetic (FM) phase to helical antiferromagnetic (HAFM) phase was observed at ∼100 K, and the two nanoscale phases coexisted up to ∼140 K. The volume fraction of the FM phase decreased with increasing temperature, eventually resulting in the formation of static magnetic solitons, which are isolated single domains of the FM phase, at around 130 K. We also performed the *in situ* observation of the HAFM phase at 142 K by applying an external magnetic field normal to the helical axis. With increasing field, a distorted HAFM phase emerged and the nanoscale phase separation between the HAFM phase and the fan phase subsequently occurred from ∼6 to ∼11 kOe. It was proven that the boundaries between these nanoscale coexisting phases were perpendicular to the z axis, which is the rotation axis common to the modulated magnetic structures.

DOI: 10.1103/PhysRevB.96.100405

Rare-earth metals and alloys provide an attractive arena for studying fundamental magnetism [1–8] since they show complex magnetic phase transitions at various temperatures and magnetic fields. The interesting magnetic structures in the intermediate magnetic phases, which exist between the high-temperature paramagnetic (PM) phase and the low-temperature ferromagnetic (FM) phase, are modulated ones, such as helical and sinusoidal structures; whereas the magnetic moments are uniform in each layer, they oscillate between the layers. These structures are mainly formed by an indirect exchange interaction between the localized $4f$ electrons through the mediation of the conduction electrons contributed by the $5d$ and $6s$ shells, known as the Ruderman-Kittel-Kasuya-Yosida coupling mechanism. Moreover, the interaction is perturbed by other magnetic interactions, such as crystal fields and magnetoelastic effects. Because the competition between the interactions depends on the temperature and magnetic field, complex magnetic phase transitions occur [1]. Detailed investigations of the modulated structures by neutron diffraction, magnetic x-ray scattering, and theoretical calculations have revealed modified tilt-helix [2], spin-slip [3], and helifan [4,5] structures.

Dysprosium (Dy) has the largest magnetic moment among the rare-earth metals: for the trivalent ion, $p_{\mathrm{eff}} = g\sqrt{J(J+1)} = 10.65\,\mu_B$, where g, J, and μ_B are the gyromagnetic factor, the total angular momentum, and the Bohr magneton, respectively. Whereas the transition between the helical antiferromagnetic (HAFM) and PM phases at T_N of ∼180 K is second order, that between the HAFM and FM phases at T_C of ∼90 K is first order [6]. The crystal structure is a hexagonal close-packed structure with $P6_3/mmc$ symmetry above T_C, whereas it is distorted orthorhombically with $Cmcm$ symmetry below T_C [7]. It was confirmed by neutron diffraction that the fan magnetic phase exists in applied magnetic fields [8]. So far, some magnetic phase diagrams have been proposed on the basis of x-ray diffraction, neutron diffraction, and measurements of physical properties such as magnetization, the magnetocaloric effect, and heat capacity; in one diagram, a spin-flop phase, a vortex phase, and a new phase are included [1,6,7].

Whereas the real-space observation of magnetic structures is valuable for understanding the complex magnetic phase transitions in rare-earth metals and alloys including Dy, such observations have seldom been reported so far. This is ascribed to the short periods, less than ∼5 nm, of the modulated magnetic structures in this system, unlike the case of the HAFM structure formed by the relativistic spin-orbit interaction, called the Dzyaloshinskii-Moriya (DM) interaction, in acentric alloys. The shortness makes the observation difficult in terms of achieving sufficient resolution. In the latter case, the HAFM structures and related structures, whose magnetic periods are more than ∼20 nm, have been investigated by real-space observation using Lorentz microscopy [9–12].

Here, we present a real-space observation of the structures in Dy by aberration-corrected Lorentz microscopy. The spatial resolution of Lorentz images is considerably reduced by the spherical aberration (C_s) and chromatic aberration (C_c) of a weakly excited Lorentz lens (LorL). To improve the resolution, we propose the use of an image C_s corrector in Lorentz microscopy [13–17]. We used an image C_s corrector and a monochromator simultaneously to reduce both of the two aberrations. The magnetic fine structure and phase separation in Dy revealed by the high-resolution (HR) Lorentz microscopy are described in this Rapid Communication.

A single crystal of the rare-earth metal Dy was mechanically cut, ground, and thinned by Ar ion milling at an acceleration voltage of 3.5 kV to obtain a transmission electron microscopy specimen. Lorentz microscopy observation was conducted with an FEI Titan cubed transmission electron microscope operated at an acceleration voltage of 300 kV and fitted with an FEI X-FEG high-brightness Schottky emitter, a Wien-filter-type monochromator, and a CEOS CETCOR hexapole-type

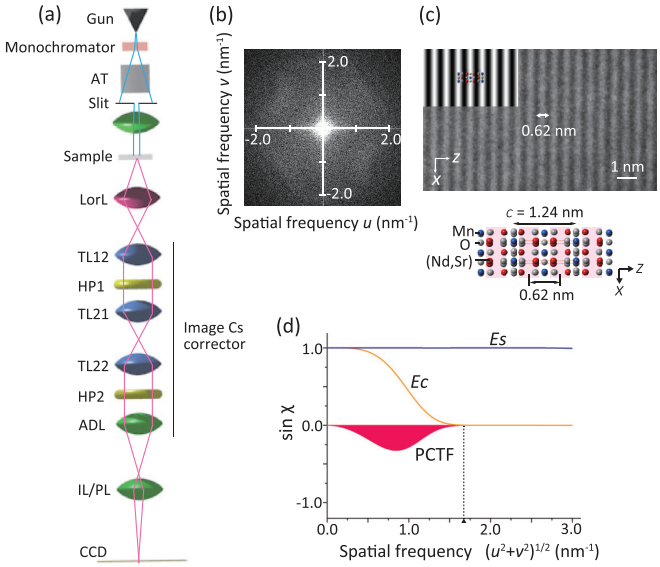

FIG. 1. Newly developed HR Lorentz microscopy using aberration correction. (a) Schematic illustration of the optical system. (b) FFT pattern of the image observed around the focus for a AuPd cross grating. (c) Image observed around the focus for the K_2NiF_4-type layered manganite $Nd_{0.2}Sr_{1.8}MnO_4$ in the [010] projection. The inset is the simulated image. The crystal structure of the manganite is shown below. (d) PCTF in the HR mode, where the defocus value is −126 nm, the Scherzer focus. E_s and E_c are envelope functions due to the convergence of the incident beam and the chromatic aberration, respectively.

image C_s corrector. The energy spread of the electron beam (ΔE) and C_c were measured using a Gatan GIF Quantum 966 energy filter. A liquid-nitrogen-type cooling holder was used for the low-temperature observation. The electron phases were retrieved from the intensity of underfocused and overfocused Lorentz images using the QPt software package (HREM Research, Inc.), which is based on the transport-of-intensity equation

$$\frac{2\pi}{\lambda}\frac{\partial I(xyz)}{\partial y} = -\nabla_{xz}\cdot[I(xyz)\nabla_{xz}\phi(xyz)],$$

where $I(xyz)$ and $\phi(xyz)$ represent the intensity and phase of electrons, respectively [18,19].

The magnetic fields were calculated from the phases using the Maxwell-Ampére equation

$$\nabla_{xz}\phi(xyz) = 2\pi et(\boldsymbol{B}\times\boldsymbol{n_1})/h,$$

where e, t, $\boldsymbol{B}$,$\boldsymbol{n_1}$, and h are the elementary electrical charge, sample thickness, magnetic field, unit vector parallel to the incident electron beam, and Planck's constant, respectively.

Figure 1(a) illustrates the optical system of the microscope. Rainbow illumination due to the energy dispersion of electrons is formed through the magnetic and electric fields of the monochromator and the accelerating tube (AT). The electrons monochromatized with the slit pass through the condenser lens system, the sample, the LorL, and the C_s corrector, where the high-order aberrations of the LorL are corrected with two hexapoles, HP1 and HP2, and three transfer lenses, TL12, TL21, and TL22. Electrons subsequently pass through

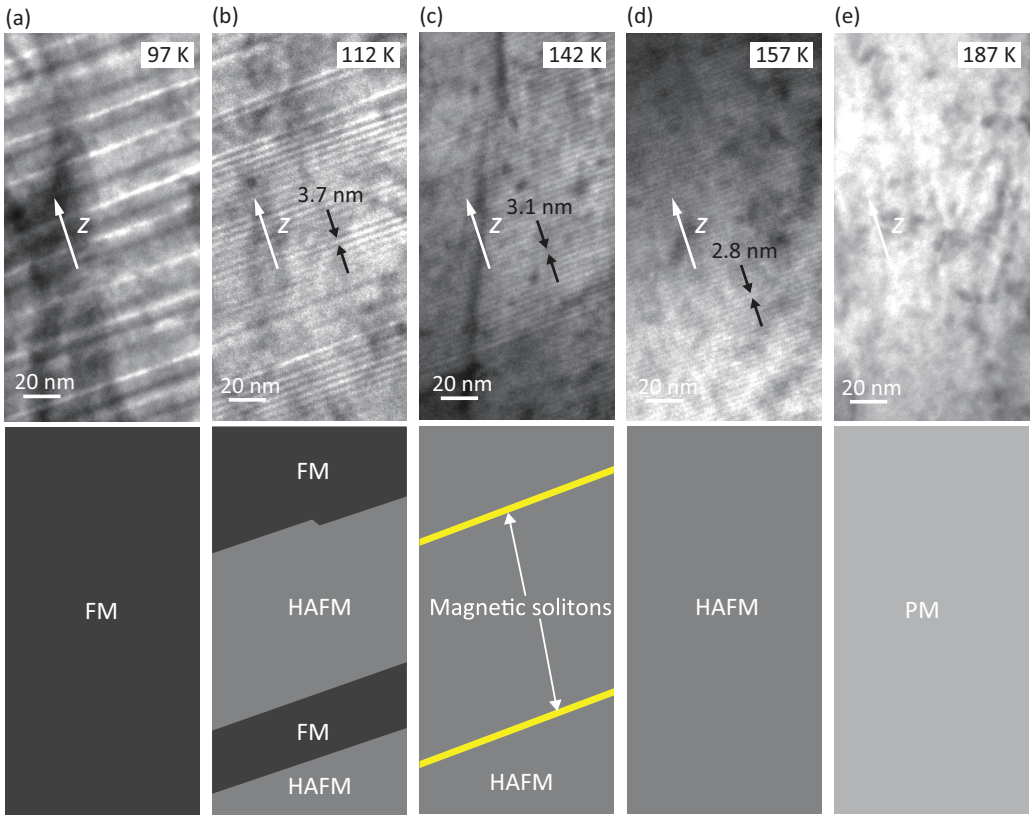

FIG. 2. Temperature dependence of Lorentz overfocused images for single-crystal Dy observed by HR Lorentz microscopy. The temperature is elevated from (a) 97 K to (e) 187 K. A schematic illustration of the areas of the corresponding FM, HAFM, and PM magnetic phases and magnetic solitons is shown below each image.

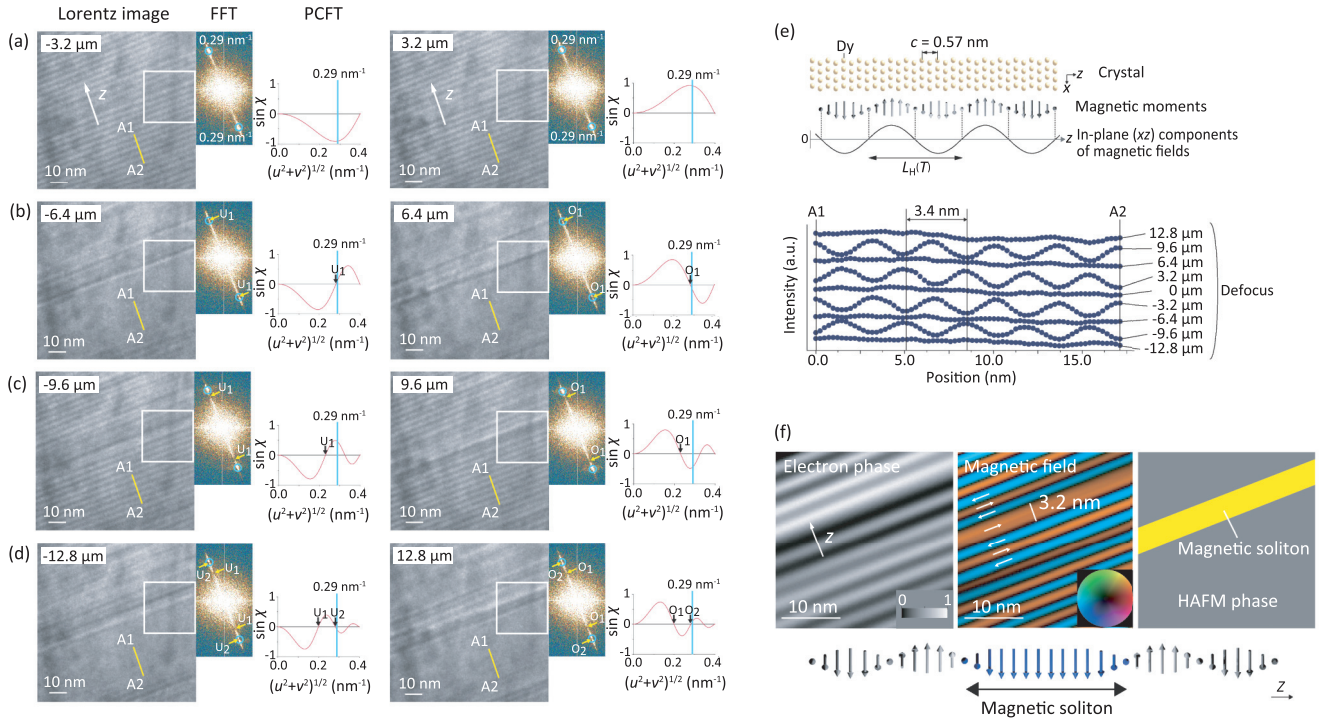

FIG. 3. (a)–(d) Series of Lorentz images observed for the HAFM phase coexisting with magnetic solitons in Dy at 127 K at defocuses from $-12.8\,\mu$m (underfocus) to $12.8\,\mu$m (overfocus), FFT patterns, and PCTFs under the defocus condition. U_1 and O_1 indicate the first zero and U_2 and O_2 indicate the second zero. The solitons are selectively imaged at defocuses of ± 6.4 and $\pm 12.8\,\mu$m. (e) Schematic illustrations of Dy crystal structure, magnetic moments, and in-plane components of magnetic fields (upper) and intensity profiles on line A1-A2 in Lorentz images in (a)–(d), where each profile is shifted along the vertical axis (lower). A periodic variation in the sinusoidal profile with the defocus is clearly seen. (f) Phase image calculated from the Lorentz images for the square area indicated in (a)–(d) (left), the obtained in-plane components of the magnetic fields (middle), and illustration of the areas of a static magnetic soliton and the HAFM phase (right). In the left image, the phase of the electron wave increases with increasing brightness, where the monotone scale indicates the relative increase from the minimum phase. In the middle image, the colors indicate the direction and magnitude of the components, as shown by the color wheel.

the adapter lens (ADL) and the intermediate and projection lens (IL/PL) system and form an image on the charge-coupled device (CCD). Figure 1(b) shows the fast Fourier transformed (FFT) pattern of the image observed around the focus for a AuPd cross grating. The maximum spatial frequency is $\sim 2\,\mathrm{nm}^{-1}$ in this HR Lorentz mode, while it is $\sim 0.5\ \mathrm{nm}^{-1}$ in the normal unmonochromated aberration-uncorrected mode. Whereas C_s, C_c, and ΔE are 8000 mm, 91 mm, and 0.88 eV in the normal mode, they are 6 mm, 91 mm, and 0.14 eV in the HR mode, respectively. We observed the layered manganite $Nd_{0.2}Sr_{1.8}MnO_4$ in the [010] projection using both modes. Although we did not observe a lattice image in the normal mode, we successfully observed a lattice image with a lattice period of 0.62 nm, which is the spacing of the MnO_2 planes, in the HR mode [Fig. 1(c)]. The phase-contrast transfer function (PCTF) in the HR mode is shown in Fig. 1(d), where the information limit is $1.7\,\mathrm{nm}^{-1}$. Magnetic fields deflect incident electrons by the Lorentz force and shift the phase of the electron wave. It is expected that a high-frequency phase shift can be recorded using the HR optical system.

In Figs. 2(a)–2(e) we show the temperature dependence of Lorentz overfocused images observed for Dy in the HR mode, where the temperature is elevated from 97 to 187 K. While FM 180° domains with the walls normal to the z axis of the crystal are formed over the entire area at 97 K, some of the FM domains are replaced by HAFM domains with a helical period of around 3.7 nm at 112 K. The helical structure is a proper screw type with the z axis as the rotation axis. The projected components of magnetization in this phase form a sine wave when the electron beam is perpendicular to the axis. The fringe spacing given by the phase in the Lorentz images corresponds to the temperature-dependent helical period $[L_H(T)]$. The boundaries between the FM phase and the HAFM phase are almost perpendicular to the z axis. The helical period decreases and the volume fraction of the HAFM phase increases with increasing temperature. The volume fraction of the FM phase decreases, resulting in the formation of static magnetic solitons, which are isolated single domains of the FM phase, at around 130 K. The magnetic solitons give fringe spacings, which are larger than the helical period of the coexisting HAFM phase in the Lorentz image. The solitons become extinct at 157 K, and the HAFM phase with a helical period of around 2.8 nm is formed over the entire area. The HAFM phase is replaced by the PM phase, which gives no magnetic contrast in the Lorentz image, at 187 K.

Figures 3(a)–3(d) show a series of Lorentz images observed for the HAFM phase coexisting with magnetic solitons at 127 K at defocuses from $-12.8\,\mu$m (underfocus) to $12.8\,\mu$m (overfocus) with the FFT patterns and the PCTFs calculated using the defocus. As shown in Fig. 3(e), the period of the

contrasts on the line A1-A2 is 3.4 nm in each image, in agreement with the helical period. However, the contrasts disappear at the defocuses of ± 6.4 and $\pm 12.8\,\mu$m. $\sin\,\chi$ is close to zero at $0.29\,\mathrm{nm}^{-1}$, which corresponds to the real-space period of 3.4 nm, in the PCTFs at these defocuses. Furthermore, the positions of bright and dark contrasts are opposite between -3.2 and $-9.6\,\mu$m and between 3.2 and 9.6 μm, corresponding to the variation of the sign of $\sin\,\chi$ at $0.29\,\mathrm{nm}^{-1}$. These features suggest that the contrast of the Lorentz images is formed through the interference between deflected electron waves. The contrasts of images observed at ± 6.4 and $\pm 12.8\,\mu$m are derived from the magnetic solitons. Only the solitons, which have different spatial frequencies from that of the HAFM phase, are selectively observed under these defocus conditions. Figure 3(f) shows the phase image calculated from the Lorentz images and the obtained in-plane components of the magnetic fields, showing the coexistence of a magnetic soliton of 3.2 nm width and a proper screw structure with the z axis as the rotation axis.

Moreover, we performed an *in situ* observation of the HAFM phase while applying an external magnetic field normal to the z axis. The external field was generated by the partial excitation of the objective lens, where the direction of excitation was opposite that of the incident electron beam. We revealed nanoscale phase separation among the HAFM phase, the distorted HAFM phase [Fig. 4(a)], in which a moment is produced along the external field, and the fan phase [Fig. 4(b)], in which the magnetic moments oscillate perpendicular to the direction of the field. Whereas the period of the distorted HAFM phase (L_D) is comparable to that of the HAFM phase, the in-plane magnetization is reduced in the former. In the fan, the moments tend to align perpendicular to the field, similarly to that in a spin-flop transition, and the period L_F is longer than L_D [8]. We can therefore identify these three phases by the magnitude of the in-plane magnetization and the period of modulation. In Figs. 4(c)–4(f), we show the field dependence of the in-plane magnetization at 142 K. The colors indicate the direction and magnitude of the magnetization, as shown by the color wheel; the magnitude decreases with decreasing brightness. Upon applying a field, a distorted HAFM phase emerged. The HAFM phase and distorted HAFM phase coexisted at 4.4 kOe, and the volume fraction of the latter phase increased with increasing intensity of the field. Moreover, the fan phase emerged from $\sim$6 kOe and the phase separation between the distorted HAFM phase and the fan phase occurred up to $\sim$11 kOe. In this regime, the volume fraction of the latter phase increased with increasing intensity of the field. The boundaries between these modulated phases are perpendicular to the z axis, which is the rotation axis of these structures.

Dissipative magnetic solitons in a wide range of nonlinear systems are currently the subject of intensive study [20–24]. More recently, a chiral magnetic soliton lattice for a helical phase created by the DM interaction in $Cr_{1/3}NbS_2$ has been observed by Lorentz microscopy [12], where a static magnetic structure with solitons arrayed at regular intervals was formed under external magnetic fields applied perpendicular to the helical axis. The helical magnetic period was rather long (48 nm at 110 K), and no magnetic inhomogeneities such as phase separation were observed in the material. On the other hand, we

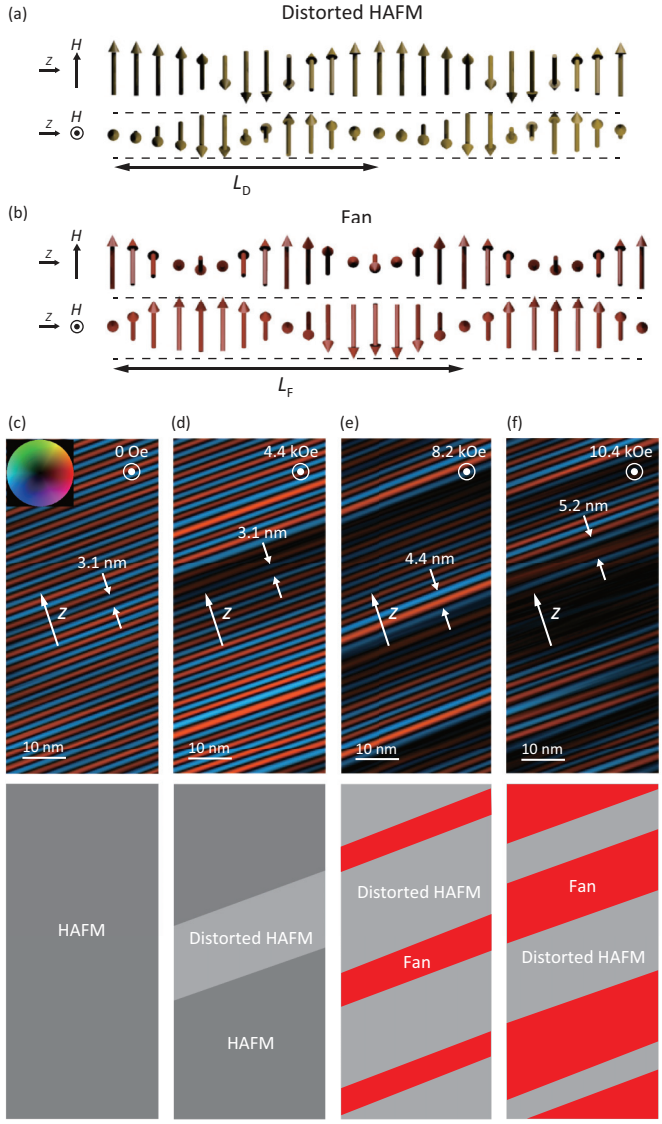

FIG. 4. (a),(b) Schematic illustrations of magnetic moments of (a) distorted HAFM phase and (b) fan phase. (c)–(f) Distributions of the in-plane magnetization obtained from Lorentz images of Dy in applied magnetic fields of up to 10.4 kOe at 142 K. The fields are normal to the z axis. A schematic illustration of the areas of the corresponding HAFM, distorted HAFM, and fan magnetic phases is shown below each distribution. It can be seen that the boundaries between these phases are perpendicular to the z axis.

revealed by HR Lorentz microscopy that static solitons exist under no field in Dy, which has a much shorter helical period of less than $\sim$5 nm. The formation of the solitons was induced by the phase transition from the FM phase to the HAFM phase; the solitons formed at the end of the phase separation between the two phases. Furthermore, external magnetic fields induced the nanoscale phase separation between the modulated magnetic phases instead of the soliton lattice. The revealed phase separation between the distorted HAFM phase and the fan phase is consistent with the results of previous mean-field and Monte Carlo calculations for Dy in applied fields: the free energies of the two phases are nearly identical, although the magnetic structures appear to be considerably different from

each other [8]. The differences in the magnetic homogeneity between Dy and $Cr_{1/3}NbS_2$ are ascribed to the difference in the magnetic interaction.

We directly observed coexisting FM and HAFM phases and static magnetic solitons in Dy under no magnetic field. It would have been difficult to reveal the temperature dependence of the size and shape of the areas and the formation of the solitons by other methods because of their low magnetic spatial resolution. Whereas the phase separation under a field was suggested in previous studies using neutron diffraction [1,8], information on the areas of the phases was not given. The present aberration-corrected Lorentz microscopy is expected to be a powerful tool for revealing unknown nanoscale and subnanoscale magnetic fine structures.

In summary, we observed the magnetic structures in Dy by aberration-corrected Lorentz microscopy. We revealed that the phase separation between the FM and HAFM phases results in the formation of static magnetic solitons under no magnetic field at around 130 K. We found that external fields of up to ∼11 kOe induced nanoscale phase separation among the HAFM, distorted HAFM, and fan phases. The boundaries of these modulated phases were perpendicular to the z axis, which is the rotation axis of these magnetic structures.

The authors thank W. Zhang and H. Usui for their support in the experiments. This work was supported by JSPS KAKENHI (Grant No. JP17K04984) and the Nanotechnology Platform of MEXT, Japan.

[1] J. Yu, P. R. LeClair, G. J. Mankey, J. L. Robertson, M. L. Crow, and W. Tian, Phys. Rev. B **91**, 014404 (2015).
[2] H. Fujii, Y. Hashimoto, T. Okamoto, N. Achiwa, and S. Kawano, J. Phys. Soc. Jpn. **50**, 2939 (1981).
[3] D. Gibbs, D. E. Moncton, K. L. D'Amico, J. Bohr, and B. H. Grier, Phys. Rev. Lett. **55**, 234 (1985).
[4] J. Jensen and A. R. Mackintosh, Phys. Rev. Lett. **64**, 2699 (1990).
[5] T. Kosugi, S. Kawano, N. Achiwa, A. Onodera, Y. Nakai, and N. Yamamoto, Physica B **334**, 365 (2003).
[6] A. S. Chernyshov, A. O. Tsokol, A. M. Tishin, K. A. Gschneidner, and V. K. Pecharsky, Phys. Rev. B **71**, 184410 (2005).
[7] A. S. Chernyshov, Y. Mudryk, V. K. Pecharsky, and K. A. Gschneidner, Jr., Phys. Rev. B **77**, 094132 (2008).
[8] N. Wakabayashi, J. W. Cable, and J. L. Robertson, Physica B **241–243**, 517 (1997).
[9] M. Uchida, Y. Onose, Y. Matsui, and Y. Tokura, Science **311**, 359 (2006).
[10] X. Z. Yu, Y. Onose, N. Kanazawa, J. H. Park, J. H. Han, Y. Matsui, N. Nagaosa, and Y. Tokura, Nature (London) **465**, 901 (2010).
[11] A. Tonomura, X. Yu, K. Yanagisawa, T. Matsuda, Y. Onose, N. Kanazawa, H. S. Park, and Y. Tokura, Nano Lett. **12**, 1673 (2012).
[12] Y. Togawa, T. Koyama, K. Takayanagi, S. Mori, Y. Kousaka, J. Akimitsu, S. Nishihara, K. Inoue, A. S. Ovchinnikov, and J. Kishine, Phys. Rev. Lett. **108**, 107202 (2012).
[13] M. Haider, S. Uhlemann, E. Schwan, H. Rose, B. Kabius, and K. Urban, Nature (London) **392**, 768 (1998).
[14] B. Freitag, M. Bischoff, H. Mueller, P. Hartel, and H. S. von Harrach, Microsc. Microanal. **15**, 184 (2009).
[15] C. Phatak, A. K. Petford-Long, O. Heinonen, M. Tanase, and M. De Graef, Phys. Rev. B **83**, 174431 (2011).
[16] T. Nagai, K. Inoke, M. Takeguchi, and K. Kimoto, Microscopy **64**, i112 (2015).
[17] S. McVitie, D. McGrouther, S. McFadzean, D. A. MacLaren, K. J. O'Shea, and M. J. Benitez, Ultramicroscopy **152**, 57 (2015).
[18] D. Paganin and K. A. Nugent, Phys. Rev. Lett. **80**, 2586 (1998).
[19] K. Ishizuka and B. Allman, J. Electron Microsc. **54**, 191 (2005).
[20] S. M. Mohseni, S. R. Sani, J. Persson, T. N. Anh Nguyen, S. Chung, Y. Pogoryelov, P. K. Muduli, E. Iacocca, A. Eklund, R. K. Dumas, S. Bonetti, A. Deac, M. A. Hoefer, and J. Åkerman, Science **339**, 1295 (2013).
[21] F. Macià, D. Backes, and A. D. Kent, Nat. Nanotechnol. **9**, 992 (2014).
[22] D. V. Dmitriev and V. Y. Krivnov, Phys. Rev. B **81**, 054408 (2010).
[23] D. Backes, F. Macià, S. Bonetti, R. Kukreja, H. Ohldag, and A. D. Kent, Phys. Rev. Lett. **115**, 127205 (2015).
[24] C. Qu, L. P. Pitaevskii, and S. Stringari, Phys. Rev. Lett. **116**, 160402 (2016).